Plume Structure and Ion Acceleration of a Helicon Plasma Source

Logan T. Williams, *Member, IEEE*, and Mitchell L. R. Walker

***Abstract*— Helicon plasma sources are capable of efficiently ionizing propellants and have been considered for application in electric propulsion. The literature suggests that the ion acceleration mechanism is a current-free double layer. Previous work shows that single-stage helicon thrusters can produce thrust in the range of 1–6 mN, but it is unknown whether the thrust contribution is due to direct ion acceleration versus thermal expansion. The ion energy and current density profiles in the plume of a helicon plasma source are measured across a range of operating conditions: 343–600 W RF power at 13.56 MHz, 50–350 G, and 1.5-mg/s Ar at a pressure of 1.6×10^{-5} torr-Ar. The plasma potential, electron temperature, and ion number density are also measured inside the discharge chamber and in the plume up to 60 cm downstream of the exit plane and 45-cm radially outward from the device axis. Ions are found to have energies in the range of 20–40 V, with total beam currents in the range of 7–47 mA. The plume has an average divergence half angle of 82°, either evenly distributed across all angles or focused at large angles to the centerline. From these measurements, it is found that the estimated thrust due to ion acceleration is far less than what has been directly measured on the same device in previous work.**

***Index Terms*— Plasma accelerators, plasma density, plasma measurements, plasma properties, plasma sources, plasma temperature.**

I. INTRODUCTION

A HELICON plasma source is a highly efficient device capable of creating a high-density, low-temperature plasma using RF waves transmitted from an antenna [1]–[7]. The proposed applications of helicon sources have included plasma processing, ion laser pumping, toroidal plasmas, and ion sources for electric propulsion. There is increased interest in the use of the helicon plasma source itself as an electrodeless thruster [8]–[16]. The primary benefit to such a device is that electrode erosion is one of the key limiters to thruster longevity; thus, an electrodeless thruster conceivably has an unlimited lifespan [10], [12]. The thrust mechanism in helicon plasma sources has been attributed either to a current-free double layer or to electron back pressure, or to both [9]–[19].

A recent work has directly measured the thrust of electrodeless helicon thrusters [20]–[24]. While there are some differences in the experimental setup and operating conditions between the investigations, the results were generally similar. Ion energy profiles consisted of two main peaks, one corresponding to the plasma potential and one corresponding to the accelerated ion beam. The energy of the ion beam population ranges between 15 and 50 V, depending on the test setup and the operating conditions, while thrust is 1–6 mN. However, it is not known to what extent the measured thrust is due to the acceleration of ions, or whether some other mechanism is primarily responsible for thrust.

The goal of this paper is to characterize the ion acceleration capability of a helicon plasma source and ascertain how the plume structure relates to the ion acceleration. There are three quantities that best capture the ion acceleration capability: the ion beam current (the amount of ions accelerated by the device per unit time), the ion energy distribution, and the beam divergence half angle. In addition, to evaluate the ion acceleration mechanism, the plasma potential, electron temperature, and ion number density are measured in the plume. Such measurements also allow comparison of the ion energy with the change in plasma potential to confirm the source of the ion energy, as well as identify any relevant structures within the plume that might impact on the ion acceleration. From these measurements, estimates of the contribution to thrust from ion acceleration can be made and compared with direct thrust measurements made previously on the same device at the same operating conditions [23], [24]. While there are multiple potential sources for thrust (ion acceleration, electron back pressure, heating of neutral gas, and magnetic nozzle effects), this paper is focused on ion acceleration through the plasma plume.

II. EXPERIMENTAL SETUP

A. Vacuum System

All experiments are conducted in vacuum test facility 1 (VTF-1). VTF-1 is a stainless steel vacuum chamber 4 m in diameter and 7 m in length. Two 3800 ft^3/min blowers and two 495 ft^3/min rotary-vane pumps evacuate the chamber to a moderate vacuum (about 30 mtorr). High vacuum is reached using six 48 diffusion pumps with a combined pumping speed of 485 000 l/s on argon. The presence of optical baffles at the inlet of the diffusion pumps reduces the effective pumping speed to 125 000 l/s. The chamber pressure is measured with a BA-571 ion gauge connected to a Varian SenTorr controller with an accuracy of 20%. An MKS type 247 four-channel readout in conjunction with an MKS 1179 mass flow controller regulates the gas flow into the helicon with an accuracy of 1% [25]. The base pressure of VTF-1 for these experiments is 1.1×10^{-5} torr.

Manuscript received November 11, 2014; revised March 7, 2015 and March 15, 2015; accepted March 23, 2015. Date of current version May 6, 2015.

The authors are with the Department of Aerospace Engineering, Georgia Institute of Technology, Atlanta, GA 30332 USA (e-mail: logan.t.williams@ieee.org; mitchell.walker@ae.gatech.edu).

Color versions of one or more of the figures in this paper are available online at http://ieeexplore.ieee.org.

Digital Object Identifier 10.1109/TPS.2015.2419211

VTF-1 has a two-axis linear motion system and a rotary table that enables the traversing of plasma diagnostics for spatial mapping. The linear tables are 1.5-m long models of the 406XR series by Parker Automation with a positional accuracy of ± 134 μm and a bidirectional repeatability of ± 3.0 μm. The rotary table is a 200RT from Parker Automation with an accuracy of ± 10 arc-min and a unidirectional repeatability of ± 0.5 arc-min.

B. Helicon Plasma Source

The helicon consists of a Pyrex discharge chamber 27.3-cm long and 14.0 cm in diameter [24], [26]. The axial magnetic field is provided by two 725-turn solenoids 7.6-cm wide with a 19.7-cm inner diameter. The solenoids are placed 10.2-cm apart. The RF signal is provided by a Yaesu FT-540 HF transceiver and amplified by an ACOM 2000A linear amplifier. An LP-100 RF wattmeter monitors the RF power transmitted and measures the standing wave ratio (SWR) with an uncertainty of ± 1 W for power and ± 0.05 for the SWR. The signal is matched by a π-type matching network. The RF power is transmitted from the transceiver to the matching network through RG-8/U coaxial cable, and from the matching network to the antenna using RG-393. The matched-line loss is 0.65 dB, which includes attenuation caused by the feedthrough. During testing, the SWR ranged from 1.01 to 1.04, which results at most in an additional 0.0004 dB of attenuation. The antenna is a double saddle antenna designed similar to the type used in [27]. The antenna is 20.3-cm long and 15.9 cm in diameter.

C. Retarding Potential Analyzer

The ion energy distribution of the thruster plume is measured with a retarding potential analyzer (RPA) [28]–[30]. The RPA consists of four grids and a collector coaxially aligned within and isolated from a stainless steel cylinder. In order from the aperture toward the collector they are the floating, electron repulsion, ion repulsion, and electron suppression grids. The floating grid has no potential applied and becomes charged to the floating potential. This serves to reduce perturbations in the plasma caused by the presence of the other biased grids. The electron repulsion grid is negatively biased with respect to chamber ground to repel plasma electrons and prevents them from reaching the collector and reducing the effective collection current. The ion repulsion grid is positively biased with respect to chamber ground to retard ions and controls what ion energies are capable of reaching the collector. The electron suppression grid has a negative potential relative to ground to repel secondary electrons emitted due to ion collisions with the collector. Since the ion repulsion grid controls the ion current collection, the probe acts as a high-pass filter, allowing only ions with energies higher than the ion repulsion grid potential to pass through to the collector. By sweeping the potential of the ion repulsion grid, a plot of the collected ion current as a function of the applied potential can be created. The negative derivative of the I–V characteristic is proportional to the ion energy distribution.

The RPA is mounted 45 cm downstream of the exit plane of the discharge chamber along the centerline of the device. At this distance the RPA is removed far enough downstream to avoid disturbing the plasma yet close enough to maintain a sufficient signal-to-noise ratio. The helicon is turned ON using the same procedure above and set to a given power, frequency, and magnetic field. The electron suppression and repulsion grids are biased 50 V below chamber ground. The ion repulsion grid bias is swept through a range of 0–120 V in 0.5 V increments six times using a Keithley 2410 SourceMeter with an accuracy of 0.12% [31]. The current collected by the probe is measured with a Keithley 6485 picoammeter, which has an accuracy of $\pm 0.1\%$ [32]. The six scans are then averaged to generate an overall I–V trace. A locally weighted scatter plot smoothing algorithm is used to smooth the data. Smoothing the data creates additional uncertainty, which is estimated as the standard deviation between the raw average and the smoothed line. The added uncertainty in the most probable energy for a population ranges from 1% to 7%, depending on how rough the raw average line is.

D. Faraday Probe

A Faraday probe consists of two primary elements: a collector and a guard ring. The collector is biased 25 V below ground to repel electrons, which ensures that the current collected by the probe is solely due to ions and not reduced by a partial electron collection. The collector is a tungsten-coated aluminum disk 22.4 mm in diameter and 6.05-mm thick. The guard ring is 25.2 mm in outer diameter with a thickness of 0.75 mm and is 5.52-cm long. A threaded rod is attached to the back of the collector and passes through the back of the probe, serving as the electrical connection. Inside the probe, the threaded rod is separated from the guard ring by a ceramic spacer [26].

The current density is measured along a semicircle with the exit plane of the thruster at the center. The total beam current can then be calculated by integrating the current density across the surface area of the hemisphere. Assuming that the plume is radially symmetric, the current density is only a function of the angle θ. With this assumption, the integration can be conceptualized as the summation of a series of infinitesimally thin circular rings of radius $r \sin\theta$ and thickness $r d\theta$. The divergence half angle, α_d, is arbitrarily defined as half of the sweep required to contain 90% of the beam current. Mathematically, this is stated as

$$0.9 I_b = \sum_{-\alpha_d}^{\alpha_d} 2\pi r^2 j(\theta) \sin\theta (\Delta\theta). \tag{1}$$

The ion beam is therefore the sum of the ion currents accelerated out of the discharge chamber. The beam divergence factor quantifies the lost thrust caused by radial ion velocity in the plume, as radial velocity in a symmetric plume has no net force contribution. Instead, the net force on the thruster is the axial component of the velocity. Thus, the beam divergence factor is defined as

$$\gamma = \cos\alpha_d. \tag{2}$$

E. Floating Emissive Probe

The basic premise of a floating emissive probe is to remove the plasma sheath between the probe and the bulk plasma and allow a direct measurement of the plasma potential. The probe utilizes a heated tungsten filament to thermionically emit electrons to break down the sheath. The filament is heated by passing a current through the filament in a floating dc circuit. As the filament current is progressively increased, the electron emission increases and decreases the difference in potential between the filament and the plasma. At a sufficient current, the sheath is completely removed and the filament floats at the plasma potential. The probe tip is constructed using a 0.127-mm-diameter thoriated tungsten wire filament inserted into a 12-cm-long double bore ceramic tube with a 1.5-mm outer diameter and 0.375-mm-diameter bores. An RF compensation box serves to choke any ac signal from contaminating the probe signal while allowing any dc signal to pass unimpeded [26]. While the plasma potential is expected to oscillate in an RF plasma, it is the time-averaged dc component that is responsible for ion drift and therefore is the value of interest [33].

F. Langmuir Probe

Langmuir probes are primarily utilized by applying a varying bias on the electrode and measuring the collected plasma current. From this I–V trace, the ion number density, temperature, and potential can be determined. However, this process is time consuming and calculation intensive. A floating emissive probe can measure the plasma potential more accurately and conveniently, but cannot alone determine density or temperature. However, if an emissive probe is used in conjunction with limited Langmuir probe measurements, the parameters can be determined. To determine electron temperature and density, there are two measurements that are needed: the floating potential, V_p, and the ion saturation current, I_{sat}. The floating potential is the potential the Langmuir probe reaches in the plasma with no applied bias or path to ground. The electron temperature can be estimated by comparing the plasma potential, V_p, measured by the emissive probe with the floating potential, since the difference in potentials is the sheath potential of the sheath surrounding the probe tip

$$V_p - V_f = -\frac{k_b T_e}{e} \ln\left(0.61\sqrt{\frac{2\pi m_e}{m_i}}\right). \quad (3)$$

However, due to cold electron emission from the probe, space charge limitations, and the formation of a double sheath around the probe, the plasma potential is larger than the raw measured potential of the probe by $0.6T_e$. The uncertainty with this method is $\pm 17\%$ [35]. The correction factor of $0.6T_e$ is lower than some other factors used in the literature, such as $1.8T_e$ [36] due to these larger factors corresponding to the thin-sheath approximation; in this paper, the Debye length to probe radius ratio is close to unity, requiring a thick-sheath approximation and a lower correction factor [37].

The ion saturation current is the current the probe collects when it is biased sufficiently negative relative to the plasma such that all electrons are repelled. Since the electron temperature ranges from 2 to 12 eV, the probe is saturated as long as it is at least 60 V below the plasma potential. The ion number density can be determined using (6) using the area of the probe, A_p

$$I_{\text{sat}} = 0.61 e n_i A_p \left(\frac{k_b T_e}{m_i}\right)^{\frac{1}{2}}. \quad (4)$$

Details about the fabrication and operation of the Langmuir probe can be found elsewhere [26].

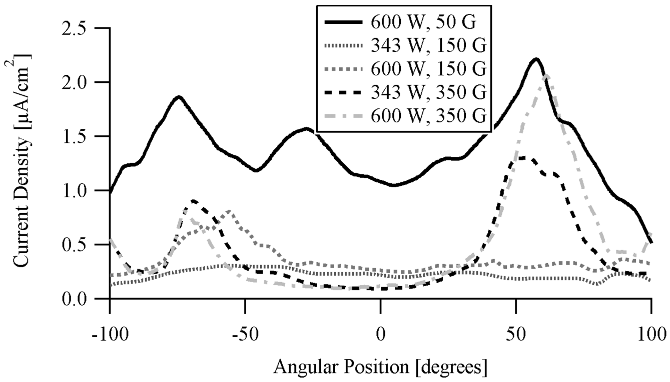

Fig. 1. Ion current density profiles as a function of power and magnetic field. Probe is 50 cm downstream, 1.5-mg/s Ar, and 1.6×10^{-5} torr-Ar.

III. RESULTS

There are three topics of interest: the trajectory of the ions accelerated, the energy of the ions, and the spatial characteristics of the plume. The distribution of ion trajectories describes the overall divergence of the ion beam generated by the plasma source as defined in (1). The spatial characteristics of the plume of interest are the plasma potential, electron temperature, and ion number density.

A. Beam Divergence

Fig. 1 shows a plot of the ion current density profiles as a function of angular position, RF power, and magnetic field strength as measured by the Faraday probe. Rather than the central peak of a collimated beam, the plume of the helicon is very broad with peaks at the wings, located at approximately 60° and −70°. The current density distribution is characterized by asymmetry, not only in the angular location of the peaks, but also in the height and number of the peaks. The 600 W, 150 G case has only one peak at −70°, while the 600 W, 50 G case has three distinct peaks: 60°, −70°, and an additional peak at −26°. The 343 W, 150 G case has no distinct peak at all and appears as a broad dispersion. Furthermore, where the 60° peak is observed, it is the largest. In the 50 G case the 60° peak is only marginally larger than the others, but the difference is quite pronounced for both cases at 350 G.

Quantifiable metrics to describe the beam divergence are difficult to obtain in this situation, as a beam half-angle generally assumes a central plume structure. Likewise, the Faraday probe generally overestimates beam current due to charge-exchange effects. However, use of this metric allows comparisons with the plume divergence of other thrusters.

TABLE I

BEAM HALF ANGLE AND BEAM CURRENT

Case	I_b (mA)	α_{90} (deg)	Uncertainty (%)
343 W, 150 G	7.20	84	12.2
600 W, 150 G	12.4	83	15.5
343 W 350 G	17.2	79	21.1
600 W 350 G	20.2	80	18.8
600 W 50 G	46.7	83	12.9

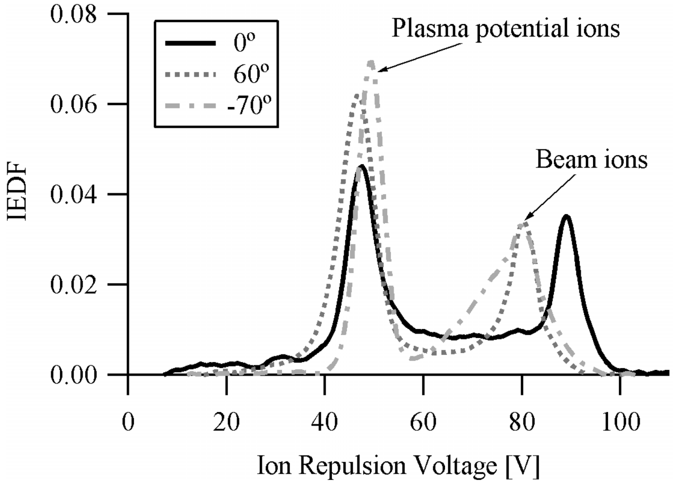

Fig. 2. Ion energy distribution at varying angular positions 50 cm from the exit plane. 600 W, 150 G, 1.5-mg/s Ar, and 1.6×10^{-5} torr-Ar.

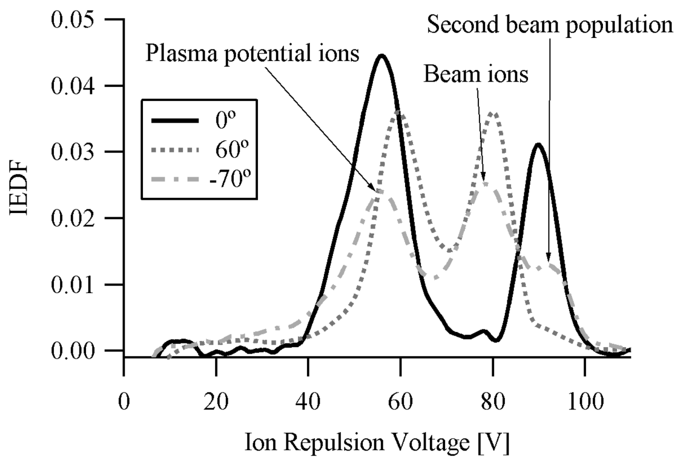

Fig. 3. Ion energy distribution at varying angular positions 50 cm from the exit plane. 600 W, 350 G, 1.5-mg/s Ar, and 1.6×10^{-5} torr-Ar.

Table I shows the beam half angles and beam currents for the five operating conditions. While the half-angle is not an ideal metric in this circumstance, the large values observed demonstrate quantitatively the broad structure of the plume. More importantly, the calculated beam currents show that the helicon does create an ion beam of significant size, especially considering that the Faraday probe is already overestimating the beam current.

B. Ion Energy

Figs. 2–4 show the ion energy distributions at each angular position of interest. A key value in energy distributions is the most probable energy, which for this application is the voltage

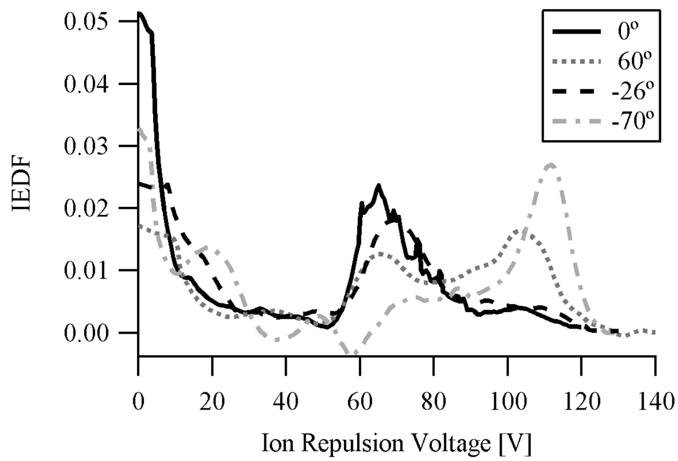

Fig. 4. Ion energy distribution at varying angular positions 50 cm from the exit plane. 600 W, 50 G, 1.5-mg/s Ar, and 1.6×10^{-5} torr-Ar.

TABLE II

MOST PROBABLE ION VOLTAGES 50 cm DOWNSTREAM

P_{RF} (W)	B (G)	θ (°)	V_{mp1} (V)	V_{mp2} (V)
343	150	0	44.5 ± 1.7	81.0 ± 3.2
		60	45.0 ± 1.8	71.0 ± 2.9
		-70	49.5 ± 2.6	73.0 ±3.8
	350	0	60.5 ± 2.3	87.0 ± 3.4
		60	57.5 ± 2.4	76.5 ± 3.2
		-70	55.0 ± 2.2	74.0 ± 3.0
600	150	0	47.5 ± 1.8	89.0 ± 3.4
		60	47.5 ± 2.1	81.0 ± 3.6
		-70	50.0 ± 1.9	80.5 ± 3.1
	350	0	56.5 ± 2.3	90.5 ± 3.7
		60	60.5 ± 2.4	81.0 ± 3.2
		-70	57.0 ± 2.2	80.0 ± 3.1

where the ion energy distribution function is maximized. Each relative maximum corresponds to an ion population distributed about that specific energy. The energy distributions for the helicon generally have two such relative maxima, or peaks. The first peak in each distribution corresponds to the plasma potential at the location of the RPA collector [12], [20]–[22]. Since the collector is grounded, ions at the plasma potential will be accelerated by the potential drop between the plasma and the collector, despite not contributing to the ion beam. Higher potential peaks correspond to accelerated ion populations. For each test case, the potential of the first peak is very similar between angular positions. Since each position is still 50 cm downstream of the exit plane, this suggests that the plasma potential should be approximately radially symmetric.

A notable trend is the change in energy distribution between the different magnetic fields. For both powers at 150 G, the first ion population is much larger than the accelerated ion propulsion. At 350 G the accelerated ion population is of a similar size or larger than the plasma potential population. The 50 G cases differ greatly from the other tested conditions, with a large population near ground in addition to the two populations corresponding to the plasma potential and the accelerated ions. The 50 G case is examined individually at a later point, and is excluded from the following discussion.

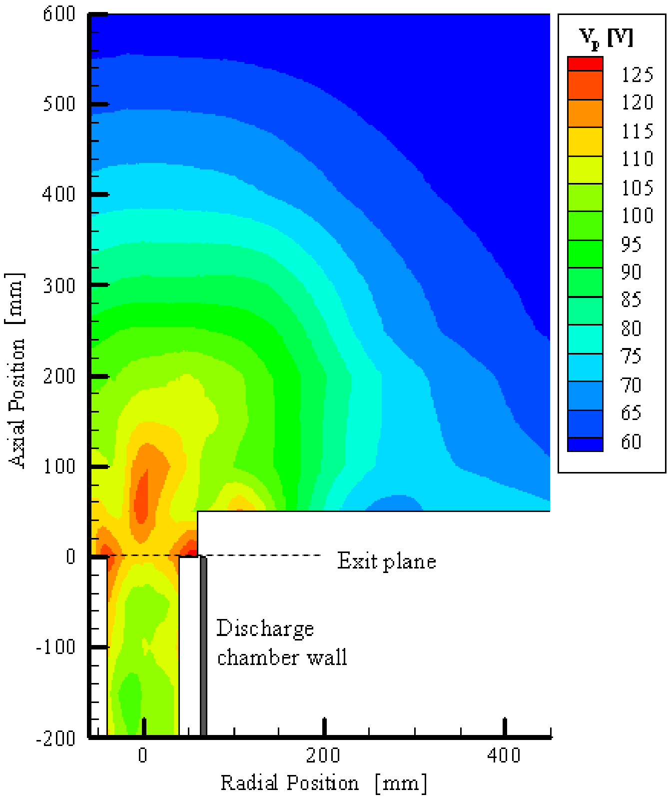

Fig. 5. Plasma potential contour at 600 W, 150 G, 1.5-mg/s Ar, and 1.6×10^{-5} torr-Ar.

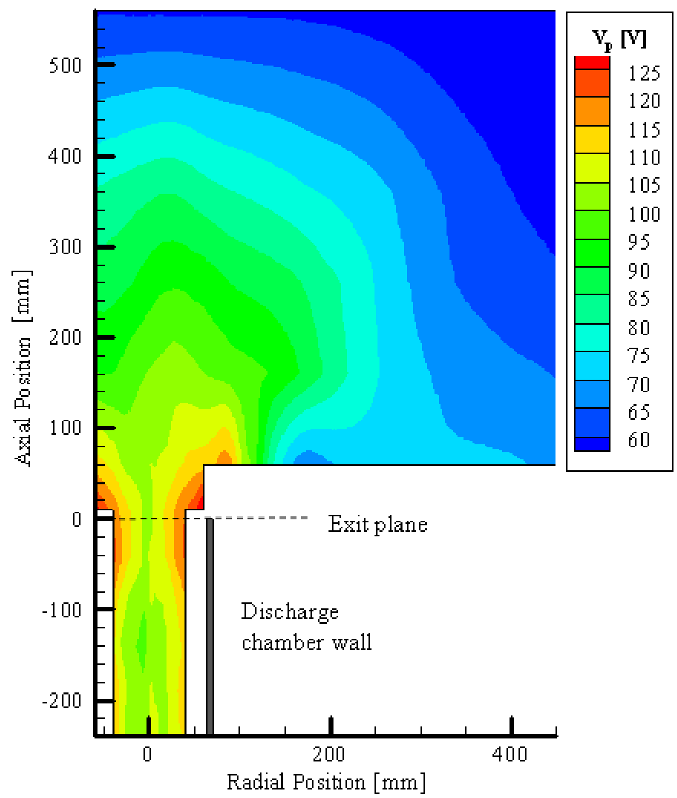

Fig. 6. Plasma potential contour at 600 W, 350 G, 1.5-mg/s Ar, and 1.6×10^{-5} torr-Ar.

A closer examination of the most probable ion voltages, shown in Table II, yields two additional trends of interest. For the same magnetic field, the first peak, representing the most probable voltage of the plasma potential, is approximately consistent across both angular position and RF power. The maximum variation among the set is 5.5 V, which is only about 2 V larger than the uncertainty of the measurements. Similarly, for the same RF power, the second most probable voltages are very similar and within the uncertainty of the RPA. The exception is that the most probable voltage on the centerline is approximately 10 V higher than on the wings. In addition, for both cases at 350 G, −70°, a third ion population is observed at the same energy as the ion beam on the centerline. This third ion population is smaller than the other two and suggests that the mechanism that reduces the ion beam energy on the wings does not affect a portion of the ions on that side.

C. Plasma Potential

Plasma potential is measured every 2 mm in the radial direction, with each radial sweep every 50 mm along the axis of the device. Figs. 5 and 6 show contour plots of the plasma potential. For the sake of brevity, only one contour plot is given for each magnetic field. The shape of the plasma potential is primarily dependent on the magnetic field, while the RF power affects the magnitude of the plasma potential. The two cases at 150 G share a similarity where the region of highest plasma potential is focused more toward the centerline of the device. This creates a convex region of high plasma potential immediately downstream of the exit plane. In contrast to the convex region of high plasma potential seen in the 150 G test cases, the 350 G data demonstrate a diverging annulus of high plasma potential around the exit plane of the discharge. This creates a converging–diverging structure out of the plasma potential centered on the exit plane of the device. As before, increasing the power increases the plasma potential while maintaining the overall shape.

In addition, there is a rise in potential closer to the wall of the discharge chamber. This is likely due to the fact that the magnetic field restricts electron but not ion radial mobility. Thus, to maintain an insulating wall boundary condition, there must be a rise in potential to limit ion flux into the wall to match electron flux due to collisional mobility. In support of this, in the 50 G case where electron mobility is much higher, there was no such rise in potential near the wall.

The 50 G case is distinct from the others in that there is no overall structure to the plasma potential either at the exit plane or downstream of it. Aside from some radial asymmetry inside the discharge chamber, the potential evenly diffuses downstream in an approximately spherical manner. Another difference between the 50 G case and the higher magnetic field tests is the far-field plasma potential is nearly 20 V lower for the 50 G condition.

A notable absence in the data is a marked drop in potential along the axis of the thruster downstream of the exit plane, which is a usual indication of a double layer [12], [13].

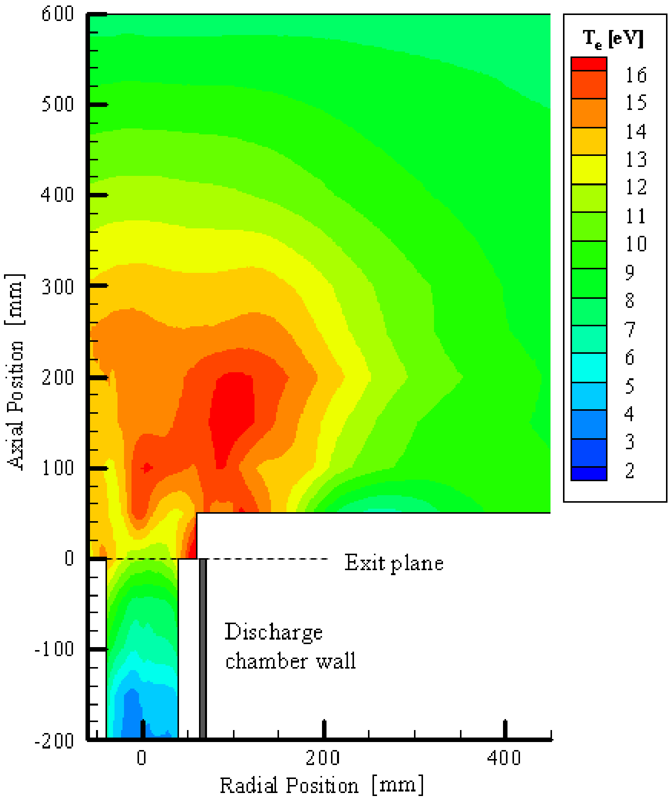

Fig. 7. Electron temperature contour at 600 W, 150 G, 1.5-mg/s Ar, and 1.6×10^{-5} torr-Ar.

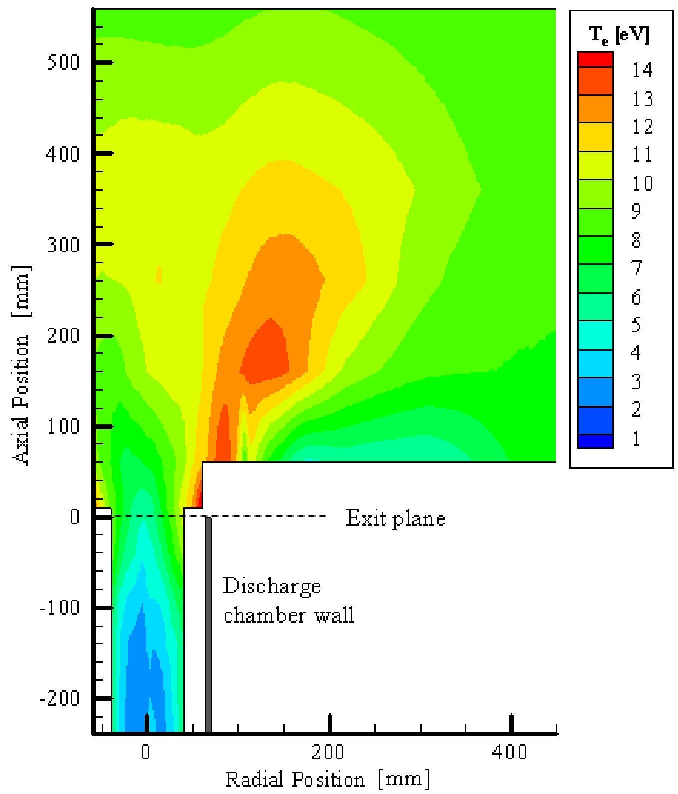

Fig. 8. Electron temperature contour at 600 W, 350 G, 1.5-mg/s Ar, and 1.6×10^{-5} torr-Ar.

This could infer that no double layer is present, but previous work has observed a similar absence of the steep drop in potential [17], [38]. One hypothesis in the literature is that the absence of this drop in potential does not necessarily infer the absence of a double layer [38]. Furthermore, there is a distinct similarity of the ion energy distributions from this paper to across previous research, regardless of the presence of the steep drop in potential [11], [14], [17], [20]–[22], [38]. This either supports the above assertion or suggests that the ion acceleration, at least in terms of magnitude (as insufficient data exist in the literature to compare Fig. 1 to), does not rely on the obvious presence of a steep drop in potential indicative of a double layer.

D. Electron Temperature

The floating potential, and thus the calculated electron temperature, is measured at the same measurement points as the plasma potential. Figs. 7 and 8 show the contours of the electron temperature. The two 150 G cases are distinguished by the downstream region of high temperature extending radially inward 100–200 mm downstream of the exit plane. In contrast to the 150 G cases, the two cases at 350 G have no regions of high electron temperature along the centerline. While the temperature still increases along the centerline from within the discharge into the plume, the centerline always maintains a lower temperature than the radial region of 60–150 mm. For the 350 G cases, the parabolic shape of the radial temperature profiles inside the discharge is maintained downstream. The only change in the radial profiles with axial distance is that as the axial position increases, the centerline increases while the edges decrease as the profile dissipates to approximately a flat line. As noted with the plasma potential, at both magnetic fields increasing the RF power has the effect of increasing the electron temperature.

It should be noted that while the temperature increases downstream of the exit plane, it should not be considered evidence of any heating or energy deposition process. Rather, due to the magnetization of the electrons in the discharge chamber, higher energy electrons are more able to break confinement closer to the exit plane, while colder electrons are carried along the diverging magnetic field lines and have a much more radial trajectory. This acts as a selective filter, passing primarily high-energy electrons, which results in a population with a higher overall average energy, and thus a higher temperature. Further downstream where this type of selection process is no longer active, the electron temperature decreases as expected.

E. Ion Number Density

Figs. 9 and 10 show the electron number density contours. Ion number density is highest along the centerline of the discharge chamber, and rapidly decreases downstream of the exit plane. The primary distinction between 150 and 350 G is that at the higher magnetic field strength the centerline density peak in the discharge chamber contains two further peaks on either side of the centerline. Another distinction is that at 350 G the ion plume extends further away from the exit plane of the discharge chamber. As a quantitative comparison,

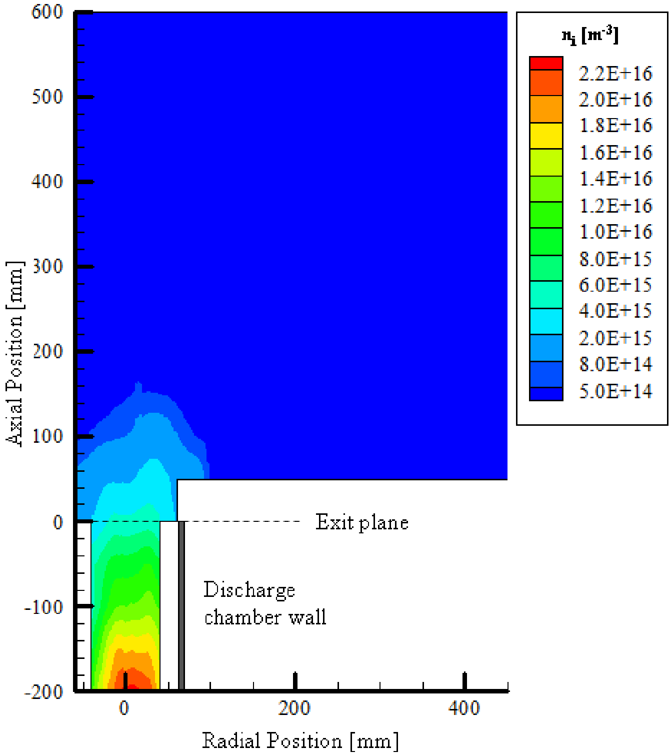

Fig. 9. Ion number density contour at 600 W, 150 G, 1.5-mg/s Ar, and 1.6×10^{-5} torr-Ar.

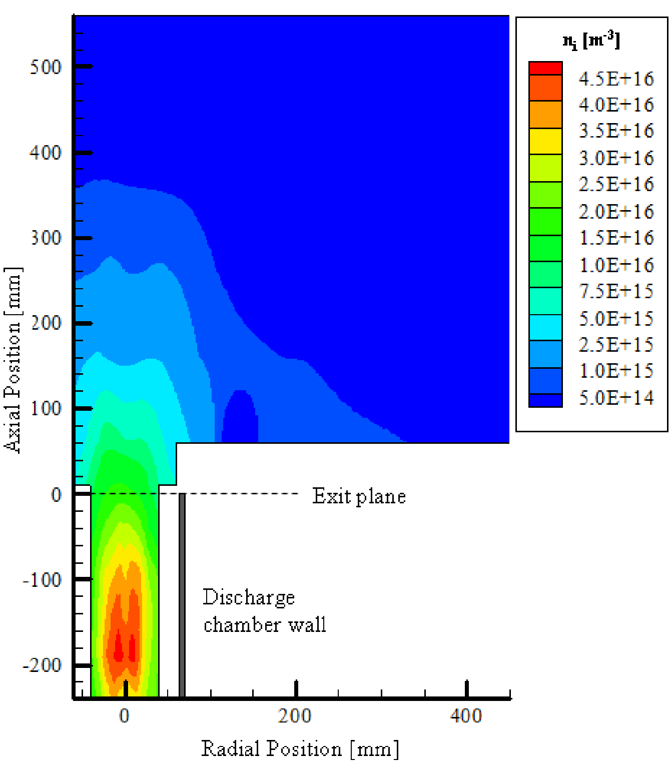

Fig. 10. Ion number density contour at 600 W, 350 G, 1.5-mg/s Ar, and 1.6×10^{-5} torr-Ar.

the plume length is defined as the distance along the centerline from the exit plane where the number density is 10% of the exit plane density. Using this metric, the plume lengths for the 150 and 350 G cases are 157 to 172 mm, respectively.

TABLE III

COMPARISON OF BEAM VOLTAGE WITH CHANGE IN PLASMA POTENTIAL

P_{RF} (W)	B (G)	θ (°)	V_b (V)	ΔV_p (V)
343	150	0	36.5 ± 3.6	32.4 ± 9.3
		60	26.0 ± 3.4	27.2 ± 9.5
		-70	23.5 ± 4.6	31.9 ± 8.8
	350	0	26.5 ± 4.1	28.9 ± 8.6
		60	19.0 ± 4.1	24.3 ± 9.1
		-70	19.0 (30.0) ± 3.7	24.2 ± 8.6
600	150	0	41.5 ± 3.9	39.5 ± 9.6
		60	33.5 ± 4.2	41.8 ± 9.4
		-70	30.5 ± 3.7	28.9 ± 8.8
	350	0	34.0 ± 4.4	42.6 ± 9.0
		60	20.5 ± 4.0	46.7 ± 8.5
		-70	23.0 (35.5) ± 3.8	43.8 ± 8.1

IV. DISCUSSION

The plume structure is captured in contours of the ion number density, plasma potential, and electron temperature, measured above. The goal of this work is to determine how the thrust contribution due to ions compares with the previously measured thrust and how the plume structure affects ion acceleration. The first task is to compare the plasma potential structure with the ion energy distributions to confirm that ion energy is dependent solely on the change in plasma potential due to a possible double layer. The second task is to identify the primary forces acting on the ions during acceleration and determine their impact on ion energy and plume divergence.

A. Ion Energy Analysis

The downstream structure of the plasma potential creates a favorable potential gradient that accelerates the ions. The electrons are accelerated through ambipolar diffusion to maintain equivalent particle flux divergence, which applies an equivalent retarding force on the ions. Due to the large mass difference between the ions and electrons, the change in ion energy is negligible. Therefore, the ion energy should be similar to the change in plasma potential from inside the discharge chamber to the location of the RPA at which the scan occurs. Since no measurements of the plasma potential are made in the radial direction past −60 mm, the change in plasma potential at −70° assumes radial symmetry of the plume and uses the data at 70°. While the plasma inside the discharge chamber is not fully symmetric, at 50 cm downstream of the contour is considerably more symmetric and makes it a reasonable assumption. The origin point for the plasma potential is selected as the point on the center axis furthest into the discharge chamber, which for most cases is −200 mm upstream of the exit plane. The beam voltage is calculated as the difference in voltage between the second and first peaks in the ion energy distribution in Table II. A comparison of the beam voltages determined from the RPA and the change in plasma potential is shown in Table III. The second value in parentheses for the beam voltage denotes the beam voltage of the third population observed in those two locations.

There is strong agreement between the beam voltage and the change in plasma potential for cases where the RPA is on

TABLE IV
ION THRUST CONTRIBUTION AND COMPONENT PARAMETERS

Operation Conditions	α (deg)	I_b (mA)	$v_{i,avg}$ (km/s)	T_{ion} (μN)
343 W, 150 G	83.5	7.20	5.97	2.02
600 W, 150 G	82.6	12.4	9.15	6.08
343 W, 350 G	79.0	17.2	7.56	10.3
600 W, 350 G	79.9	20.2	8.16	12.0

the centerline. Off the centerline, the ion energy measured by the RPA is generally lower than the change in plasma potential. This suggests that ions exhausted at an angle dissipate some of the electrostatic energy as they are accelerated. The case of 343 W, 350 G at −70° has two populations above the plasma potential. While the second beam voltage is actually higher than the change in plasma potential at that point, this is within the uncertainty of the emissive probe and the RPA. The cause of the energy loss for ions accelerated at an angle can be further investigated by examining the electric field in the plume region.

The thrust generated through ion acceleration can be defined as

$$T = \gamma \frac{m_i}{e} I_b \bar{v}_i \tag{5}$$

where the average ion velocity is calculated from the ion energy distributions

$$\bar{v}_i = \frac{\sum_{j=k+1}^{100} x_j \left(\frac{2e(V_j - V_p)}{m_i}\right)^{\frac{1}{2}}}{\sum_{j=k+1}^{100} x_j} \{k|V_k = V_p\}. \tag{6}$$

Equation (6) V_j is the voltage of the jth step of the voltage sweep, and x_j is the value of the probability distribution function at that voltage. The overall average ion velocity of each operating condition is the mean of the average ion velocities at the three angular positions. Using the average ion velocities along with the results in Table I, the thrust contribution by ion acceleration is calculated and shown in Table IV.

The results show that ion contribution to thrust is several orders of magnitude lower than the measured thrust. As a comparison, the cold gas thrust of the various propellant flow rates is in the range of 0.5–2 mN. This shows that very little of the power coupled to the helicon is transferred to the axial ion energy. Even if the beam divergence factor is neglected, the ion thrust contribution only increases by a factor of 5–8, which still results in a negligible thrust contribution. The average ion velocity yields an expected specific impulse of approximately 600–900 s, but in practice the ionization fraction and beam currents are so low that the thrust contribution from the ion beam is negligible. It is much more likely that the primary thrust contribution is a combination of collisional heating of the neutral propellant and the resulting thermal exhaust, along with electron back-pressure on the discharge chamber [39].

B. Electric Field Effects

Since the primary source of the ion energy comes from the plasma potential structure, the accelerating electric field can be determined from the negative gradient of the potential across the area of the contour. The electric field is calculated using Newton's Difference Quotient of the measured plasma potential. Since the plasma potential is given in two dimensions, the radial and axial components of the field are solved individually

$$E_{r,i} = \frac{\phi_{i+1} - \phi_{i-1}}{r_{i+1} - r_{i-1}} \tag{7}$$

$$E_{z,i} = \frac{\phi_{i+1} - \phi_{i-1}}{z_{i+1} - z_{i-1}}. \tag{8}$$

Under the assumption that the plume is radially symmetric, there is no azimuthal variation of the plasma potential; therefore, there is no azimuthal electric field. While this is most likely not true, any variation in θ should be small compared with variations in r and z. Thus, only the radial and axial electric fields are considered.

One item to note from the overlay is that the electric field has very strong radial components near the exit plane of the discharge chamber and in the region where r is greater than 100 mm. The presence of these radial electric fields potentially explains the high degree of divergence within the plume, as an ion exiting the discharge chamber would encounter a large radial electric field unless it is on the centerline of the device.

One particular structure in the electric field occurs at the radial position 75 mm and axial position between 100 and 150 mm. At this point, there is a cluster of electric field lines that turn from purely axial to mostly radial, and some field lines turn back toward the thruster. The cause of this field line cluster can be seen by overlaying the electric field onto the contour for the electron temperature, shown in Fig. 11.

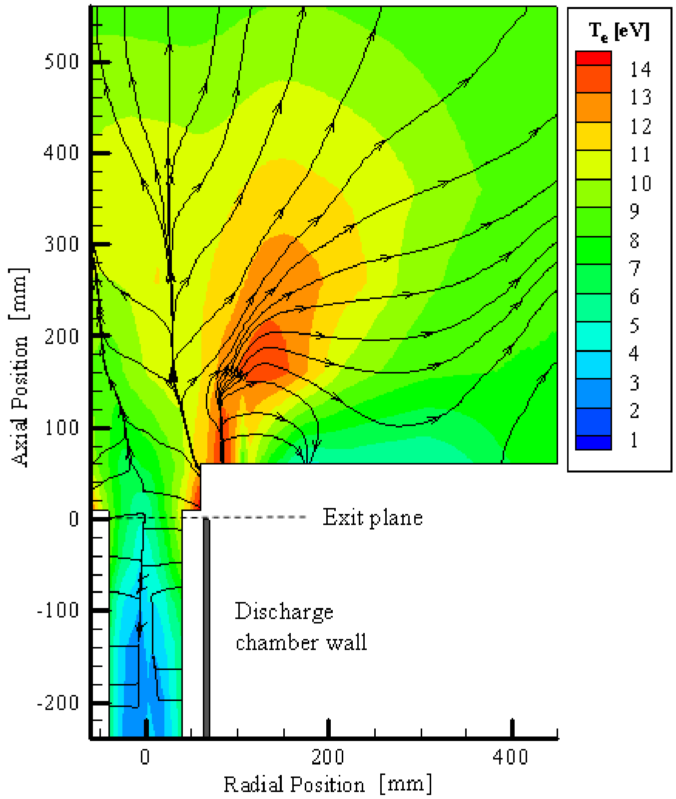

Fig. 11. Electron temperature and electric field lines at 600 W, 350 G, 1.5-mg/s Ar, and 1.6×10^{-5} torr-Ar.

The field line cluster occurs at the high electron temperature region observed in the previous chapter. This region is most likely formed from high-energy electrons escaping confinement on the magnetic field lines. The lower energy electrons remain confined and are turned back toward the thruster, which pulls the electric field lines back in the $-z$-direction.

The above field structure would explain the high degree of beam divergence in the 600 W, 350 G case, and by extension the 343 W, 350 G case, as the two have similar electron temperature contours. Any ion that enters the high electron temperature regions would be accelerated radially outward, and for certain regions receive a negative axial component as well. Conversely, at 150 G the high electron temperature regions are more broadly spread across the radius of the plume. This suggests that the electric field lines are more evenly distributed, which promotes a wide plume with ions emitted evenly across all angles.

This mechanism also explains the current density distribution of the 50 G case. Recall that while the 50 G case has distinct peaks, the relative values of the peaks compared with the baseline current density are not as disparate as in the 350 G cases. At 50 G, the electrons are only weakly magnetized and only a very small region of high electron temperature forms near the exit plane. While these regions still direct some ions radially outward, it is much less pronounced. Thus, the current density distribution is generally even with a few regions of higher current. The cause of the $-26°$ peak is difficult to determine, as no data are available for that side of the plume. However, it is most likely the result of asymmetry within the temperature contour. It is worth noting that the central region of low electron temperature favors that side of the plume, so it is possible that this asymmetry causes the $-26°$ peak.

C. Ion Trajectories

Thus far, the discussion has been limited to a qualitative assessment of the observed contours of the plasma potential and the electron temperature with overlays of the electric field lines. While the electric field is an important component in determining the ion path, it does not describe the pathlines of the ions. Therefore, to quantitatively discuss the effects of the operating conditions, the ion trajectories must be determined. A Lagrangian approach is used to generate ion trajectories by solving the momentum equations for a single ion placed at the exit plane of the discharge chamber. The momentum equations can be iteratively solved through discrete time steps until the ion reaches the edge of the measured data set, recording the position at each time step. This generates a pathline for the ion, and by solving for multiple starting positions, a sample of the ion trajectories can be generated.

For this model, all variations in the azimuthal direction are neglected, as radial symmetry is assumed. The ions are considered to be isothermal at 0.1 eV. The momentum equation from the MHD equations is

$$nm_i\left[\frac{\partial \vec{v}_i}{\partial t} + (\vec{v}_i \cdot \nabla)\vec{v}_i\right] = en_i(\vec{E} + \vec{v}_i \times \vec{B}) - \nabla(n_i k_b T_i) + m_i n_i v_{\text{in}}(\vec{v}_n - \vec{v}_i). \tag{9}$$

Electron–ion collisions are neglected, as the calculated mean free path is found to be much larger than that of ion-neutral collisions. The term on the left-hand side of the equation is the material derivative, which is only used in the Eulerian approach. This is easily converted into a Lagrangian system utilizing the definition of the total derivative. Due to radial symmetry and the fact that $E \times B$ drift is small compared with the electric field, the azimuthal ion velocity is negligible. This also removes all $1/r$ terms, eliminating a singularity on the centerline axis. The resulting radial and axial momentum equations are

$$\frac{dv_{i,r}}{dt} = \frac{e}{m_i}E_r - \frac{e}{m_i}v_{i,z}B_\theta - \frac{k_b T_i}{m_i n_i}\frac{\partial n_i}{\partial r} \tag{10}$$

$$\frac{dv_{i,z}}{dt} = \frac{e}{m_i}E_z - \frac{e}{m_i}v_{i,r}B_\theta - \frac{k_b T_i}{m_i n_i}\frac{\partial n_i}{\partial z}. \tag{11}$$

The collisional term is dropped since it applies to a bulk fluid element, not to an individual particle. While ion-neutral collisions are no longer captured in the trajectory model, they should not be removed from qualitative consideration, as will be discussed later. The azimuthal magnetic field term is also neglected; since the solenoids provide no azimuthal magnetic field, this field would only be induced by plasma currents. Initial estimates of this term using the MHD equations found this term to be much smaller than the electric field or pressure terms, and is therefore neglected to simplify the calculations. In addition, only motion in the rz plane is modeled, as under the radial symmetry assumption any ion that drifts out of the plane of the page will be replaced by one drifting into the plane. Furthermore, the $E \times B$ drift is small compared with the magnitude of the electric field, which means any azimuthal drift is negligible, as previously stated. In essence, the model is a 2-D projection of the ion pathlines through the plume.

Equations (10) and (11) are solved iteratively in time steps of 5 μs, and the values of the plasma parameters are interpolated from the measured data using bilinear interpolation. The interpolated value of some parameter f at a position of (r, z) is given by

$$\begin{aligned} &f(r,z)\\ &= \frac{1}{(r_2 - r_1)(z_2 - z_1)}\\ &\quad \times [f(r_1, z_1)(r_2 - r)(z_2 - z) + f(r_2, z_1)(r - r_1)(z_2 - z)\\ &\qquad + f(r_1, z_2)(r_2 - r)(z - z_1) + f(r_2, z_2)(r - r_1)(z - z_1)] \end{aligned} \tag{12}$$

where $r_2 > r > r_1$, and $z_2 > z > z_1$, and the numbered coordinates correspond to positions of measured data points. The position and the velocity are incremented each step by

$$\delta r = \frac{1}{2}\frac{dv_{i,r}}{dt}(\delta t)^2 + v_{i,r}\delta t \tag{13}$$

$$\delta z = \frac{1}{2}\frac{dv_{i,z}}{dt}(\delta t)^2 + v_{i,z}\delta t \tag{14}$$

$$\delta v_{i,r} = \frac{dv_{i,r}}{dt}\delta t \tag{15}$$

$$\delta v_{i,z} = \frac{dv_{i,z}}{dt}\delta t. \tag{16}$$

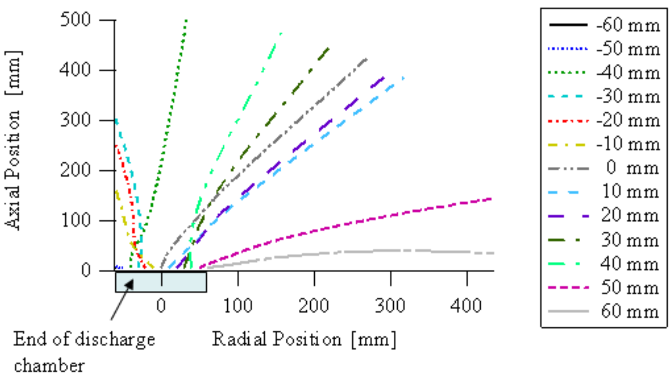

Fig. 12. Simulated ion pathlines for various initial radial positions at 600 W, 50 G.

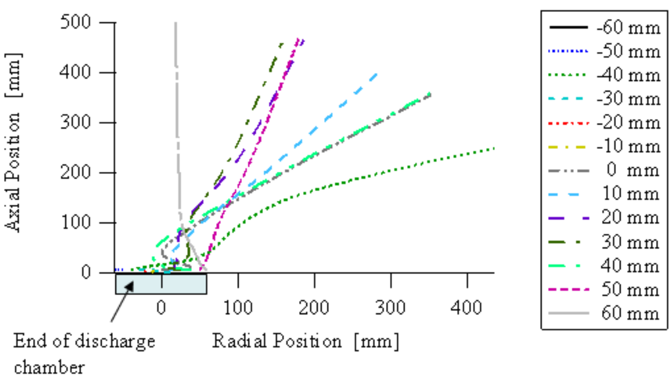

Fig. 13. Simulated ion pathlines for various initial radial positions at 343 W, 150 G.

Most parameters of the model are set by the measured data of the plume, but there are a few assumed initial conditions. The ions are assumed to start at an initial axial position of 5 mm past the exit plane of the discharge chamber. This allows enough calculation space to determine whether ions backstream into the discharge chamber or accelerate downstream. A sample set of ions are modeled with varying initial radial positions, from −60 to 60 mm in 10-mm steps. The ions are assumed to have an initial thermal velocity at 0.1 eV (approximately 500 m/s) in both the radial and axial velocity components. Ions with a negative initial radial position are initialized with a negative radial velocity, and ions with a positive initial radial position have a positive radial velocity. All ions are assumed to have a positive axial velocity. Variation of the initial velocities shows that the model is generally insensitive to initial ion energies within the range of reasonable estimates (less than 2 eV) due to the large electric fields.

The trajectories for a sample of ion initial positions are shown in Figs. 12–14. Only one simulation per magnetic field is shown, as the shape of the data contours is strongly set by the magnetic field and other parameters are less significant. At 50 G the trajectories are evenly spread, though ions placed close to the walls near the high electron temperature region have highly radial trajectories. As the magnetic field increases, the trajectories begin to be focused more radially outward, until at 350 G very few trajectories are primarily axial. Some of the ions are found to be immediately accelerated back into

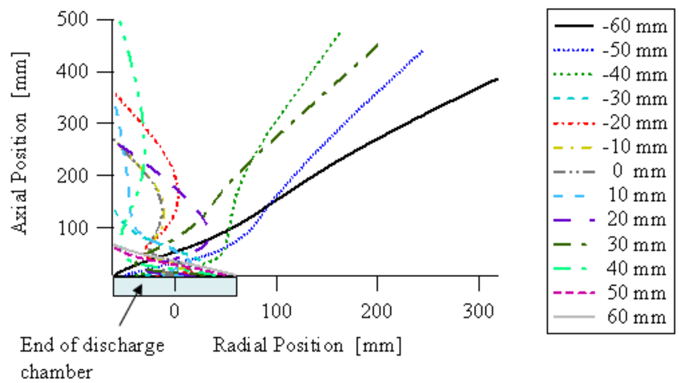

Fig. 14. Simulated ion pathlines for various initial radial positions at 600 W, 350 G.

the discharge chamber. This is caused by the initial position of the ion being placed near an adverse potential gradient.

There are several noteworthy observations regarding the simulations. First, the momentum equation is heavily dominated by the electric field. The temperature and the density of the ions are low enough such that the pressure gradient term is smaller than the electric field term for the entire trajectory. Second, the effect of the magnetic field on ion trajectories explains the behavior of the current density profiles in Fig. 1. At a low magnetic field strength, the ions have a much more even distribution of resultant path angles. Ions at the center tend to exit at an angle, and combined with a density distribution that peaks on the centerline, this results in current density peaks at these angles. However, these current density peaks are smaller relative to the average current density compared with peaks in the other operating conditions. At higher magnetic fields the ion trajectories become much more focused on these off-center angles, which results in the formation of large peaks relative to the average.

A third observation is that the predicted trajectories are at angles less than 60° as observed by the Faraday probe. However, this discrepancy is due to the exclusion of ion-neutral collisions in the model. These collisions are most prevalent inside the discharge chamber and just beyond the exit plane. Using a simulation of the neutral gas expansion out of the discharge chamber [40], [41], the ion-neutral mean free path grows from approximately 50 mm at the exit plane to 150 mm at 50 mm downstream of the exit plane. After this point, the mean free path rapidly increases until the plume becomes effectively collisionless. A plot of the mean free path as a function of position is shown in Fig. 15.

Ion-neutral collisions will dissipate ion energy, either through momentum exchange or through charge-exchange, although the momentum exchange collision cross section is larger for momentum exchange [42]. As a result, the majority of collisional dissipation of ion energy will occur within the first 100 mm from the exit plane of the discharge chamber.

The region near the exit plane shows negligible net radial motion. For the 50 G case, this is a result of the electric field having negligible radial components immediately downstream of the exit plane, excluding the small regions near the walls. For the 150 and 350 G cases, this is a result of the ions reflecting between the regions of high plasma potential that

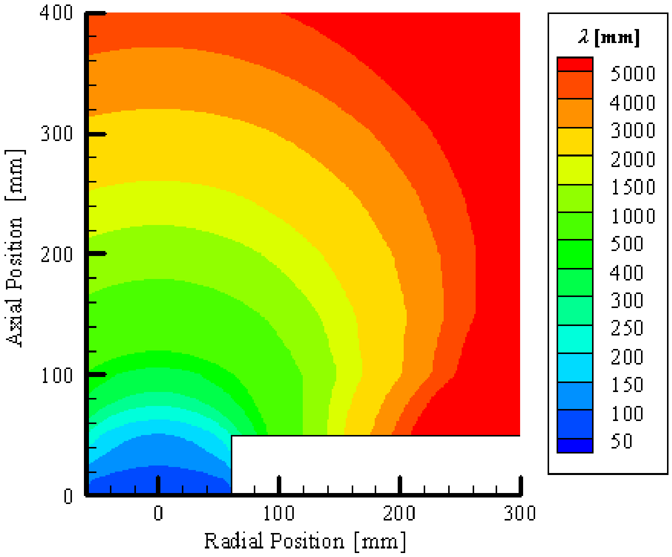

Fig. 15. Simulated ion-neutral mean free path for 1.5-mg/s Ar flow.

extends from the walls downstream. The 350 G case in particular subjects ions to multiple reflections. Thus, ions in this region generally undergo a net axial acceleration, while any radial components are primarily added further downstream near the regions of high electron temperature that occur 100 mm downstream of the exit plane and beyond. Therefore, as ions exit the discharge chamber, collisional dissipation of ion energy primarily impacts on the axial velocity of the ions. This has an impact on the ion trajectories by increasing the relative size of the radial component, which increases the trajectory divergence angle from the centerline. Therefore, the high beam divergence angle observed is most likely caused by a combination of radial electric field lines downstream of the exit plane and collisional dissipation of axial energy close to the exit plane.

The oscillatory trajectories in the 350 G case also explain another discrepancy. Recall from Table III that the operating conditions that saw the greater disagreement between the beam voltage measured by the RPA and the difference in plasma potential is at 350 G. The 350 G is also where the greatest amount of radial ion reflection occurs near the exit plane of the discharge chamber. The electric field is a conservative force, which means that the total energy gained by the ion is independent of the path taken. This is quantified by the change in plasma potential between the inside of the discharge chamber and 50 cm downstream at the RPA. However, collisional dissipation is nonconservative, which means that as the path length of the ion trajectory increases inside the region close to the exit plane, the amount of energy dissipated increases. The ions accelerated out of the discharge chamber at 350 G have a much longer path inside this collisional region than at 150 or 50 G. Therefore, a greater amount of energy is lost, which explains why the ion that reaches the RPA has a lower energy than predicted solely by the plasma potential.

V. Conclusion

There are three performance metrics that are used to evaluate ion acceleration: ion energy, beam current, and the beam divergence half angle. In all the three metrics, the helicon plasma source demonstrated ion acceleration that is far below that found in contemporary electric propulsion devices. The ion energies observed are presumed to be a result of a current-free double layer caused by plasma expansion from a high-density region in the discharge chamber to a low-density region in the plume. This only results in a beam voltage in the range of 20–40 V. In addition, the beam current is generally less than 20 mA, which suggests that the double layer allows only a limited number of ions to exit the discharge chamber. Furthermore, the shape of the plasma plume structure, which determines the ion trajectories, is strongly affected by the magnetic field. At low magnetic fields the relatively symmetric plasma expansion yields a diffuse plume with an even distribution of ion trajectories. At higher magnetic fields the ions tend to be deflected off centerline at large angles. Utilizing these performance metrics, the estimated thrust contribution from ions is 2–12 μN, which is far below the 1–6 mN previously measured and suggests that ion acceleration is not the primary thrust mechanism. From these findings, it can be concluded that a helicon plasma source functions essentially as an ion source and not as an ion accelerator, for the purposes of propulsive application.

Acknowledgment

The authors would like to thank American Pacific In Space Propulsion for their support, the Georgia Tech Aerospace Engineering Machine Shop for fabrication and hardware support, as well as the students of the High-Power Electric Propulsion Laboratory for additional assistance. The authors would also like to thank R. Boswell for assistance rendered in correspondence and conversation.

References

[1] F. F. Chen, "Plasma ionization by helicon waves," *Plasma Phys. Controlled Fusion*, vol. 33, no. 4, pp. 339–364, 1991.
[2] F. F. Chen, "Helicon plasma sources," in *High Density Plasma Sources*, O. A. Popov, Ed. Park Ridge, NJ, USA: Noyes, 1995.
[3] F. F. Chen, "Experiments on helicon plasma sources," *J. Vac. Sci. Technol.*, vol. 10, no. 4, pp. 1389–1401, 1992.
[4] R. W. Boswell, "Very efficient plasma generation by Whistler waves near the lower hybrid frequency," *Plasma Phys. Controlled Fusion*, vol. 26, no. 10, pp. 1147–1162, 1984.
[5] A. W. Degeling, C. O. Jung, R. W. Boswell, and A. R. Ellingboe, "Plasma production from helicon waves," *Phys. Plasmas*, vol. 3, no. 7, pp. 2788–2796, 1996.
[6] A. J. Perry, D. Vender, and R. W. Boswell, "The application of the helicon source to plasma processing," *J. Vac. Sci. Technol.*, vol. 9, no. 2, pp. 310–317, 1991.
[7] A. W. Degeling, T. E. Sheridan, and R. W. Boswell, "Intense on-axis plasma production and associated relaxation oscillations in a large volume helicon source," *Phys. Plasmas*, vol. 6, no. 9, pp. 3664–3673, 1999.
[8] T. Ziemba, J. Carscadden, J. Slough, J. Prager, and R. Winglee, "High power helicon thruster," in *Proc. 41st AIAA/ASME/SAE/ASEE Joint Propuls. Conf. Exhibit*, Tucson, AZ, USA, Jul. 2005, paper AIAA 2005-4119.
[9] C. Charles, "A review of recent laboratory double layer experiments," *Plasma Sour. Sci. Technol.*, vol. 16, no. 4, p. R1, 2007.
[10] R. W. Boswell *et al.*, "Helicon double layer thrusters," in *Proc. 29th Int. Electr. Propuls. Conf.*, Princeton, NJ, USA, 2005, paper IEPC-2005-290.
[11] C. Charles, R. W. Boswell, and M. A. Lieberman, "Xenon ion beam characterization in a helicon double layer thruster," *Appl. Phys. Lett.*, vol. 89, no. 26, p. 261503, 2006.

[12] M. D. West, C. Charles, and R. W. Boswell, "Testing a helicon double layer thruster immersed in a space-simulation chamber," *J. Propuls. Power*, vol. 24, no. 1, pp. 134–141, 2008.
[13] C. Charles and R. W. Boswell, "Current-free double-layer formation in a high-density helicon discharge," *Appl. Phys. Lett.*, vol. 82, no. 9, pp. 1356–1358, 2003.
[14] C. Charles and R. W. Boswell, "Laboratory evidence of a supersonic ion beam generated by a current-free 'helicon' double-layer," *Phys. Plasmas*, vol. 11, no. 4, pp. 1706–1714, 2004.
[15] C. Charles, "Hydrogen ion beam generated by a current-free double layer in a helicon plasma," *Appl. Phys. Lett.*, vol. 84, no. 3, pp. 332–334, 2004.
[16] W. Cox, C. Charles, R. W. Boswell, and R. Hawkins, "Spatial retarding field energy analyzer measurements downstream of a helicon double layer plasma," *Appl. Phys. Lett.*, vol. 93, no. 7, p. 071505, 2008.
[17] B. W. Longmier *et al.*, "Ambipolar ion acceleration in an expanding magnetic nozzle," *Plasma Sour. Sci. Technol.*, vol. 20, no. 1, p. 015007, 2011.
[18] A. Fruchtman, "Electric field in a double layer and the imparted momentum," *Phys. Rev. Lett.*, vol. 96, p. 065002, Feb. 2006.
[19] A. Fruchtman, "Double layer and thrust," in *Proc. Bull. Annu. Meeting*, vol. 50. 2005, p. 109.
[20] J. Ling, M. D. West, T. Lafleur, C. Charles, and R. W. Boswell, "Thrust measurements in a low-magnetic field high-density mode in the helicon double layer thruster," *J. Phys. D, Appl. Phys.*, vol. 43, no. 30, p. 305203, 2010.
[21] K. Takahashi *et al.*, "Direct thrust measurement of a permanent magnet helicon double layer thruster," *Appl. Phys. Lett.*, vol. 98, no. 14, p. 141503, 2011.
[22] S. Pottinger, V. Lappas, C. Charles, and R. Boswell, "Performance characterization of a helicon double layer thruster using direct thrust measurements," *J. Appl. Phys. D, Appl. Phys.*, vol. 44, no. 23, p. 235201, 2011.
[23] L. T. Williams and M. L. R. Walker, "Thrust measurements of a helicon plasma source," in *Proc. 47th AIAA/ASME/SAE/ASEE Joint Propuls. Conf. Exhibit*, San Diego, CA, USA, Aug. 2011, paper AIAA 2011-5893.
[24] L. T. Williams and M. L. R. Walker, "Thrust measurements of a radio frequency plasma source," *J. Propuls. Power*, vol. 29, no. 3, pp. 520–527, 2013.
[25] *MKS Product Specifications, MKS 1179A Instruction Manual*, MKS Instruments, 2000, p. 57.
[26] L. T. Williams, "Ion acceleration mechanisms of helicon thrusters," Ph.D. dissertation, Dept. Aerosp. Eng., Georgia Inst. Technol., Atlanta, GA, USA, 2013.
[27] K.-K. Chi, T. E. Sheridan, and R. W. Boswell, "Resonant cavity modes of a bounded helicon discharge," *Plasma Sour. Sci. Technol.*, vol. 8, no. 3, pp. 421–431, 1999.
[28] R. R. Hofer, "Development and characterization of high-efficiency, high-specific impulse xenon Hall thrusters," Ph.D. dissertation, Dept. Aerosp. Eng., Univ. Michigan, Ann Arbor, MI, USA, 2004.
[29] L. B. King, "Transport-property and mass spectral measurements in the plasma exhaust plume of a Hall-effect space propulsion system," Ph.D. dissertation, Dept. Aerosp. Eng., Univ. Michigan, Ann Arbor, MI, USA, 1998.
[30] I. H. Hutchinson, *Principles of Plasma Diagnostics*. Cambridge, U.K.: Cambridge Univ. Press, 1987.
[31] *Keithley Product Specifications Keithley 2400 Series Sourcemeter Instruction Manual*, Keithley Instruments, Cleveland, OH, USA, 1998.
[32] *Keithley Product Specifications Keithley 6485 Picoammeter Instruction Manual*, Keithley Instruments, Cleveland, OH, USA, 2001.
[33] J. Kang, R. N. Carlile, and J. F. O'Hanlon, "A radio frequency compensated emissive probe," *Rev. Sci. Instrum.*, vol. 67, no. 5, pp. 1818–1821, 1996.
[34] L. A. Schwager, W. L. Hsu, and D. M. Tung, "Effects of cold electron emission on the plasma sheath," *Phys. Fluids B, Plasma Phys.*, vol. 5, no. 2, pp. 621–630, 1996.
[35] B. M. Reid, "The influence of neutral flow rate in the operation of Hall thrusters," Ph.D. dissertation, Dept. Aerosp. Eng., Univ. Michigan, Ann Arbor, MI, USA, 2009.
[36] J. P. Sheehan, Y. Raitses, N. Hershkowitz, I. Kaganovich, and N. J. Fisch, "A comparison of emissive probe techniques for electric potential measurements in a complex plasma," *Phys. Plasmas*, vol. 18, no. 7, p. 073501, 2011.
[37] Y. Raitses, D. Staack, A. Smirnov, and N. J. Fisch, "Space charge saturated sheath regime and electron temperature saturation in Hall thrusters," *Phys. Plasmas*, vol. 12, no. 7, p. 073507, 2005.
[38] C. S. Corr, J. Zanger, R. W. Boswell, and C. Charles, "Ion beam formation in a low-pressure geometrically expanding argon plasma," *Appl. Phys. Lett.*, vol. 91, no. 24, pp. 241501-1–241501-3, 2007.
[39] A. Fruchtman, "Neutral depletion in a collisionless plasma," *IEEE Trans. Plasma Sci.*, vol. 36, no. 2, pp. 403–413, Apr. 2008.
[40] C. Cai, "Theoretical and numerical studies of plume flows in vacuum chambers," Ph.D. dissertation, Dept. Aerosp. Eng., Univ. Michigan, Ann Arbor, MI, USA, 2005.
[41] S. Giannelli, A. Kieckhafer, and M. L. R. Walker, "Neutral gas expansion in a cylindrical helicon discharge chamber," *J. Propuls. Power*, vol. 29, no. 3, pp. 540–546, 2013.
[42] A. V. Phelps, "Cross sections and swarm coefficients for nitrogen ions and neutrals in N_2 and argon ions and neutrals in Ar for energies from 0.1 eV to 10 keV," *J. Phys. Chem. Ref. Data*, vol. 20, no. 3, pp. 557–573, 1991.

Logan T. Williams (M'09) received the B.S. degree in mechanical engineering, and the M.S. and Ph.D. degrees in aerospace engineering from the Georgia Institute of Technology, Atlanta, GA, USA, in 2006, 2009, and 2013, respectively.

He was a Graduate Research Assistant with the High Power Electric Propulsion Laboratory, Atlanta, from 2006 to 2013. He has been a Propulsion Engineer with Praxis Inc., Alexandria, VA, USA, since 2013, where he has been involved in micro-propulsion and miniature hydraulics.

Mitchell L. R. Walker received the B.S.E., M.S.E., and Ph.D. degrees from the University of Michigan, Ann Arbor, MI, USA, in 1999, 2000, and 2004, respectively, all in aerospace engineering.

He is currently an Associate Professor with the Georgia Institute of Technology, Atlanta, GA, USA. He has extensive design and testing experience with Hall thrusters and ion engines, and performed seminal work in Hall thruster clustering and vacuum chamber facility effects. He also serves as a Corporate Consultant around his area of expertise in top-tier organizations, such as Newell-Rubbermaid, Atlanta, Lockheed Martin, Bethesda, MD, USA, and National Aeronautics and Space Administration, Washington, DC, USA. His primary research interests include electric propulsion, plasma physics, and hypersonic aerodynamics/plasma interaction. His current research interests include theoretical and experimental work in advanced spacecraft propulsion systems, diagnostics, plasma physics, helicon plasma sources, space debris mitigation, magnetoplasmadynamic thrusters, and pulsed-inductive thrusters.